Recovering and monitoring the thickness, density and elastic properties of sea ice from seismic noise recorded in Svalbard

Agathe Serripierri[1], Ludovic Moreau[1], Pierre Boue[1], Jerome Weiss[1], and Philippe Roux[1]

[1]Institut des Sciences de la Terre, Université Grenoble Alpes, Grenoble, France

Correspondence: Ludovic Moreau (ludovic.moreau@univ-grenoble-alpes.fr)

Abstract. Due to global warming, the decline in the Arctic sea ice has been accelerating over the last four decades, with a rate that was not anticipated by climate models. To improve these models, there is the need to rely on comprehensive field data. Seismic methods are known for their potential to estimate sea-ice thickness and mechanical properties with very good accuracy. However, with the hostile environment and logistical difficulties imposed by the polar regions, seismic studies have remained

5 rare. Due to the rapid technological and methodological progress of the last decade, there has been a recent reconsideration of such approaches. This paper introduces a methodological approach for passive monitoring of both sea-ice thickness and mechanical properties. To demonstrate this concept, we use data from a seismic experiment where an array of 247 geophones was deployed on sea ice in a fjord at Svalbard, between March 1 and 24, 2019. From the continuous recording of the ambient seismic field, the empirical Green's function of the seismic waves guided in the ice layer was recovered via the so-called 'noise

10 correlation function'. Using specific array processing, the multi-modal dispersion curves of the ice layer were calculated from the noise correlation function, and then inverted for the thickness and elastic properties of the sea ice via Bayesian inference. The evolution of sea-ice properties was monitored for 24 days, and values are consistent with the literature, as well as with measurements made directly in the field.

1 Introduction

15 In the alarming context of global warming, modern climatology faces the challenging task of updating climate models for more reliable forecasting. However, these models rely on parameters that are changing at an accelerating rate. One of these parameters is the extent and thickness of the Arctic sea ice, which have been declining faster than expected for the last four decades (Stroeve et al, 2007; Rampal & al., 2011). A worrying example is the change between the forecast from 2012 to 2019: in 2012, a sea-ice-free Arctic was anticipated sometime after 2050 (Stroeve et al, 2012; Steffen et al, 2018), while in

20 2019, this was modified to as early as 2030 (Screen and Deser, 2019). The evolution of the extent of the sea ice is subject to thermodynamic processes that are affected by important parameters, such as the mechanical properties and thickness of the ice. Hence, continuous and accurate monitoring of these parameters is essential in view of the need to update our climate models.

Currently, given the challenging logistics for accessing the Arctic, satellite remote sensing remains the preferred approach to monitor the thickness of sea ice (Kwok , 2010; Wadhams, 2012). This approach relies on conversion from the sea-ice freeboard

25 distribution into an average thickness, on the assumption that the density of the ice is known. However, this results in high

uncertainties that are due to a number of factors: (i) strong dependence of this approach on models of ocean elevation and the difficulty to correct for fluctuations in the altitude of the ocean surface (Kwok and Cunningham , 2008; Petty & al., 2020); (ii) the presence of snow, which complicates the measurement of the freeboard (Kwok and Cunningham , 2008); and (iii) important temporal and spatial variations in the density of the ice and snow. For example, thin first-year ice (*i.e.*, less than 1-m thick) is

30 typically more porous and contains more brine than thick, multiyear ice. Consequently, depending on the assumptions used to estimate the sea-ice freeboard, and on which density the conversion is made from, estimations of the same sea-ice thickness can vary from 0.2 m to 1.2 m (Ricker & al., 2014; Mu & al., 2018).

While satellite remote sensing solves the problems associated with logistics and allows the monitoring of sea-ice thickness over the whole Arctic Basin, this is at the cost of high uncertainties and poor temporal and spatial resolution. Hence, comple-

35 mentary approaches are needed to improve the monitoring of sea ice. Satellite data can be combined with data acquired in the field, *e.g.*, from upward-looking sonar acquisitions or electromagnetic surveys (Lindsay and Schweiger , 2015; Belter & al , 2020).

The use of seismic methods to study sea ice has been considered for more than 60 years, but due to the hostile environment in polar regions, such studies have remained rare. This is despite their potential for very accurate estimations of the ice thickness,

40 h, density, ρ, Young's modulus, E, and Poisson's ratio, ν (Anderson , 1958; Hunkins, 1960; Yang and Giellis, 1994; Stein et al, 1998). The main limitation for seismic methods used to be the transport of the seismic stations. However, with the miniaturisation of electronic components and the rapid progress in terms of battery life, it is currently possible to easily transport small autonomous geophones (*e.g.*, less than 1 kg for one geophone) that can record a seismic field for several months. Another limitation was the need for a human presence in the field to proceed with acquisitions using active seismic

45 sources. Seismic methods based on noise interferometry (Shapiro and Campillo, 2004; Sabra et al., 2005) have solved this problem, and seismic acquisitions applied to sea ice are now possible without the need of human intervention, other than for the installation and removal of the geophones (Marsan et al, 2012, 2019; Moreau, Boué et al, 2020; Moreau, Weiss et al, 2020). Another seismic method that was presented by Romeyn & al. (2021) makes it possible to estimate the thickness of sea ice. This consists of exploiting the propagation of air-coupled flexural waves that are excited by an impulsive seismic source. Romeyn

50 & al. (2021) suggested that these waves might be naturally excited by icequakes produced by natural cracking of the ice, which thus provides a complementary approach to existing passive methods for estimation of ice thickness.

Based on laboratory-scale data, in Moreau et al (2017), we introduced a methodology where the frequency-wavenumber spectrum of seismic guided waves propagating in an ice layer was used to infer h, E, and ν with very high accuracy. In Moreau, Boué et al (2020), this methodology was successfully applied to field data acquired in March 2019 in the Van Mijen

55 Fjord in Svalbard (Norway), after the frequency-wavenumber spectrum was obtained from noise interferometry via the so-called 'noise correlation function' (NCF). The NCF is obtained by correlating the ambient seismic noise recorded between station pairs of an array of geophones. It can be shown that it converges toward the impulse response of the medium, which for sea ice is a superposition of seismic modes guided through its thickness. Estimations of h, E, and ν were obtained from these data, and we concluded that this approach is suitable for long-term monitoring of sea ice. Building on this work, the

60 methodology was improved in view of automatic, more accurate, and more complete monitoring of the ice in the Van Mijen Fjord.

The first improvement concerns the calculation of the NCF. We introduce a method based on beamforming (Rost & Thomas, 2002) for detection and selection of only the time windows where the seismic noise source is aligned with the station pair used, which significantly improves the signal-to-noise ratio (SNR) of the NCF. The second improvement concerns the inversion

65 strategy. In Moreau, Boué et al (2020), E and ν were determined from the velocity of the longitudinal and shear horizontal guided waves. The values were then used in a finite element (FE) model for computing synthetic wavefields. However, we noted that a joint inversion of the three parameters E, ν, and h is computationally too expensive for forward modeling with a FE model. With these two improvements, we obtained the daily evolution of the thickness and elastic parameters of the sea ice.

The present paper, we use the analytical model introduced in Stein et al (1998) for generating synthetics. This approach

70 is computationally very efficient, so Bayesian inference can be used for joint inversion of E, ν, and h, and also the additional parameter ρ (see section 2.4.2). The evolution of these parameters reveals a constant increase in the ice thickness between March 1 and 24, 2019, while the mechanical parameters remained stable.

2 Instruments and methods

Contrary to wave propagation in an infinite and homogeneous domain, propagation in a waveguide (*i.e.*, a thin, bounded

75 domain, such as an ice layer) is subject to multiple reflections at the upper and lower bounds. This causes interference that results in several propagating guided modes that are similar to the Lamb modes that propagate in a stress-free plate (Lamb, 1917). However, the nature of the seismic field in sea ice is modified by the presence of the solid-liquid interface. In the following, we use the terminology introduced in Moreau, Boué et al (2020) to describe the modes in the wavefield:

- the fundamental quasi-symmetric mode (QS_0), which produces mainly longitudinal motion;

80 - the quasi-Scholte mode (QS), which produces mainly flexural motion;

- the fundamental mode (SH_0), which produces shear-horizontal motion.

Guided modes are dispersive, and hence seismic signals recorded in sea ice away from the source are distorted. An important property of guided wave propagation is the relationship between the dispersion curves of the guided modes and the mechanical properties and thickness of the ice. The dispersion curves are the representation of the modal propagation in the frequency-

85 wavenumber space, which requires measurement of the wavefield with an array of sensors. In the following section, we only recall the main features of this array, but the reader can refer to Moreau, Boué et al (2020) for a detailed description.

2.1 Seismic array

The experiment was conducted on fast ice in the Van Mijen Fjord, which is located on the southern coast of the island of Spitsbergen, in the Norwegian archipelago of Svalbard (Fig. 1a). More precisely, the seismic array was deployed on Lake

90 Vallunden, which is connected to the fjord by a channel and is surrounded by moraines. The town of Sveagruva is located not far to the northwest (Fig. 1a).
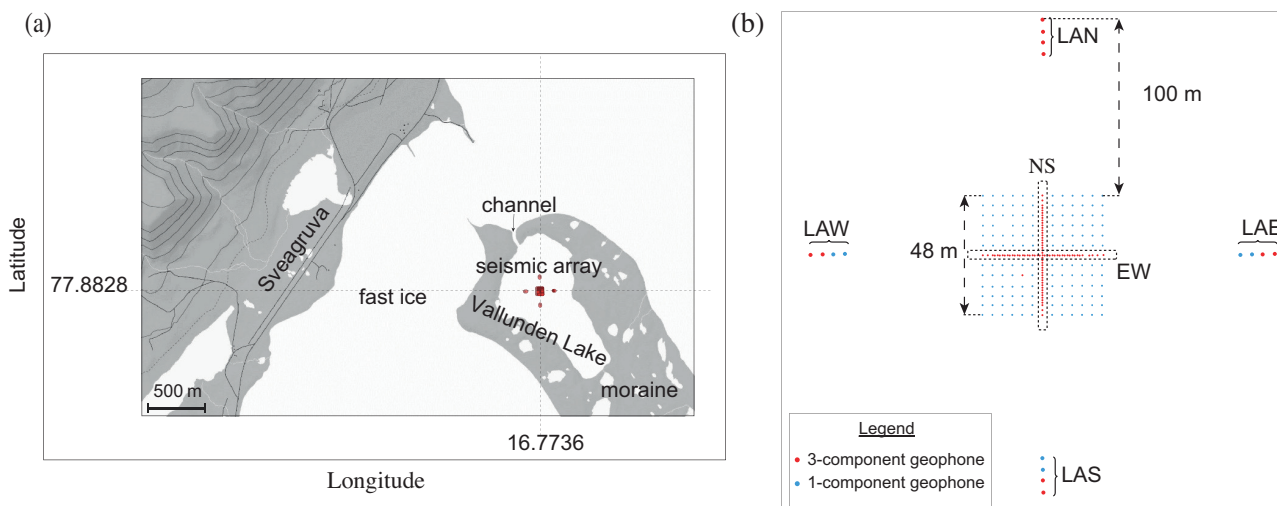
Figure 1. (a) Map of the area where the seismic array was installed (red) on Lake Vallunden, Svalbard, which is naturally bounded by moraines and connected to Van Mijen Fjord by a small channel. The town of Sveagruva is located about 1 km northwest of the array. (b) Schematic representation of the seismic array. The red dots indicate the three-component (3C) geophones and the blue dots indicate the one-component (1C) geophones. In the main array, the 1C geophones are spaced by 4 m, and the 3C geophones are organized in a dense cross with 1 m spacing oriented along the east-west (EW) and north-south (NS) directions. To the east, north, south, and west there are linear arrays of four geophones (LAE, LAN, LAS, LAW).(a) modified from (Moreau, Boué et al, 2020).

The seismic network is a mix between one-component (1C; Fig. 1b, red dots) and three-component (3C; Fig. 1b, blue dots) FairFieldNodal Zland geophones. It consists of a dense array of geophones with 4 m spacing that forms a square. Within this square there is an even denser cross of 3C geophones. The first two geophones at the edges of this cross are spaced 2 m apart, and all of the others along the cross have a regular spacing of 1 m. The two lines of geophones that form this dense cross are referred to as the east-west (EW) line and the north-south (NS) line. To the east, west, north, and south of the array there are extra antennae of four sensors that are referred to as linear array east (LAE), west (LAW), north (LAN), and south (LAS). In the following, LAN and LAS (Fig. 1b) are used as virtual sources for the receivers in the NS line, while LAE and LAE are used as virtual sources for the receivers in the EW line.

The structure of this deployment was designed with a spatial sampling and geometry that allowed the QS_0 and SH_0 modes to be measured up to about 250 Hz, and the QS mode to be measured up to about 150 Hz Moreau, Boué et al (2020). Moreover, all of the data used in this work are sampled with a sampling frequency of 500 Hz (Moreau et RESIF , 2019).

2.2 Noise correlation function

2.2.1 The noise correlation function

105 For the last 15 years, developments of passive seismological methods have shown that it is possible to extract the medium properties from seismic-noise interferometry without the need for active sources (*e.g.*, sledgehammer, explosions, vibrating truck) or earthquakes. The NCF is obtained by correlation of continuous recordings of seismic noise from a pair of seismometers, and it has been shown to converge toward an estimate of the elastodynamic Green's function between the seismometers (Campillo & Paul , 2003; Shapiro and Campillo, 2004; Sabra et al., 2005). This conversion of passive sensors into virtual active sources

110 is very useful in modern seismology for monitoring and tomography purposes. However, theoretical hypotheses that ensure convergence of the NCF toward the Green's function are restrictive, as they require noise sources to be stationary and with an isotropic distribution, and signals to be recorded over an infinitely long time (Lobkis & Weaver , 2001; De Verdière , 2006). In practice, these hypotheses are of course never fulfilled. Nonetheless, the seismic noise is very rich in our dataset: it includes the thousands of icequakes that occur every day, directional anthropogenic noise (*e.g.*, other field experiments in the fjord, human

115 activities near Sveagruva), and seismic noise associated with the wind and water currents. Hence the Green's function can be precisely estimated (Campillo & Paul , 2003; Shapiro and Campillo, 2004) with adequate pre-processing of the data.

A usual way of calculating the NCF when sources are not isotropic and/or not stationary consists of truncating the continuous recordings of a station pair into shorter noise segments, and to inter-correlate these segments before averaging the correlations. The segment lengths should be such that seismic sources are as stationary as possible within the segments. With the present

120 dataset, we checked that a length of 5 min is appropriate.

2.2.2 Optimization of the noise correlation function using beamforming

As the distribution of seismic sources is not isotropic every day, we propose to optimize the retrieval of the Green's function by selecting for each day of the recording all of the noise segments for which the energy comes from a direction that is within $\pm\,10°$ of the lines of orientation (Fig. 2, red dashed line). The choice of $\pm\,10°$ for the direction of the sources is because this

125 aperture is small enough for the emitted wavefield to be localised in the end-fire lobes. These are the areas on either side of the ends of the receiver line in which the phase of the wave correlation function is stationary with respect to the azimuth (Roux & al, 2004). The aperture of these lobes depends on the ratio between the wavelength and the distance between the receivers (Gouédard , 2008).

To determine the direction of the seismic sources in each noise segment, classical beamforming is applied to the data (Rost

130 & Thomas, 2002). In some noise segments, seismic sources have different directions for different frequency bands. To prevent the inclusion of these segments in the NCF, we apply the beamforming in several frequency bands, to select only the segments for which the direction of the source is stable independent of the frequency. This processing is based on the spatial coherence between the receivers. Therefore, spatial sampling must satisfy the Nyquist criterion. The 1C geophones have a spatial sampling of 4 m. This sets the minimum wavelength that can be spatially sampled to 8 m, which is that of mode QS at a frequency of 16

135 Hz. Applying beamforming at frequencies higher than 16 Hz would cause aliasing problems. Hence, we define four frequency
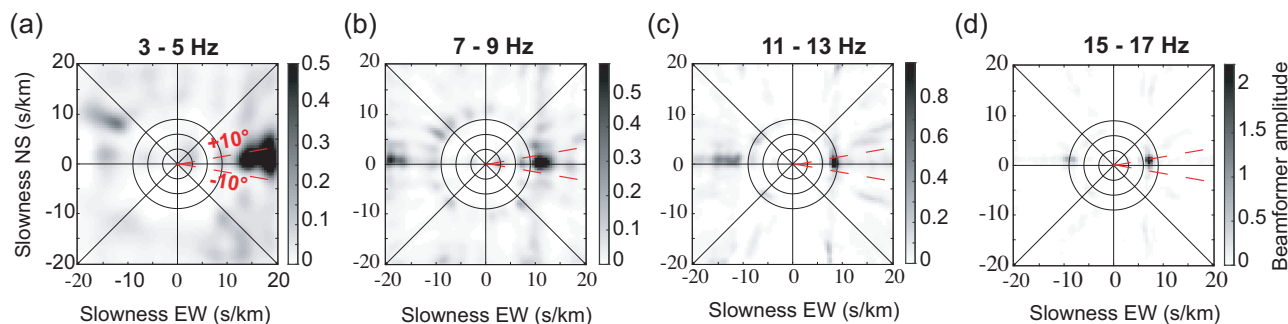
Figure 2. Beamforming obtained from the ambient seismic noise recorded on March 9, 2019, over a 5-min window from 3:50 am in four frequency bands: (a) [3-5] Hz; (b) [7-9] Hz; (c) [11-13] Hz; (d) [15-17] Hz. The dominant source is located within $\pm 10°$ (red dashed lines) in the EW sensor line.

bands for selection of the appropriate noise segments: [3-5] Hz, [7-9] Hz, [11-13] Hz, and [15-17] Hz. The direction of the dominant noise source can be identified in each frequency band; *e.g.*, Figure 2 shows the beamforming of a noise segment in all frequency bands. A seismic source from the east is detected, and this segment is therefore selected for calculation of the NCF between the virtual sources of LAE and the receivers of line EW.

140   Finally, the optimized NCF is obtained by correlation of the selected noise segments and averaging of these correlations. This process is illustrated in Figure 3. Figure3a shows the NCF of all of the 5-min noise segments obtained from the correlation between a virtual source of LAE and the receiver at the centre of the EW line (Figure 1b). The segments selected for the beamforming are shown in color in Figure3a, and the rejected segments (*i.e.*, those showing a superposition of sources that originate from several directions outside the end-fire lobes) are shown in black and white. Indeed, another research team was

145 working in the Vallunden Lake to the north west of our experimental area. This generated many dominant sources from this direction, and impacted upon our seismic array negatively, with a source that was not included in the end fires lobes of our two reception directions, EW and NS. Figure 3b shows the beamforming calculated from all of the 5-min segments (on the left) and that of the selected segments (on the right). Figure 3c shows a comparison between a NCF obtained by averaging the correlations from all of the noise segments (blue waveform) and that obtained by averaging only the selected segments (red

150 waveform). The SNR is significantly improved, especially at early arrival times, where unfavorable noise source directions corrupt the NCF. When calculating the dispersion curves, this introduces a bias in the frequency-wavenumber spectra (see section 2.3), and the modes appear to propagate faster than they actually do. This results in degraded estimates of the sea-ice properties.

2.3   Extraction of the frequency-wavenumber spectra from the noise correlation function

155 To infer the sea-ice properties, the inverse problem is based on a minimization of the difference between the dispersion curves measured *in situ*, and those obtained synthetically. It is therefore necessary to extract the optimal dispersion curve for each mode. To this end, we used the method introduced in Minonzio & al (2010) in the field of medical ultrasound, and applied in
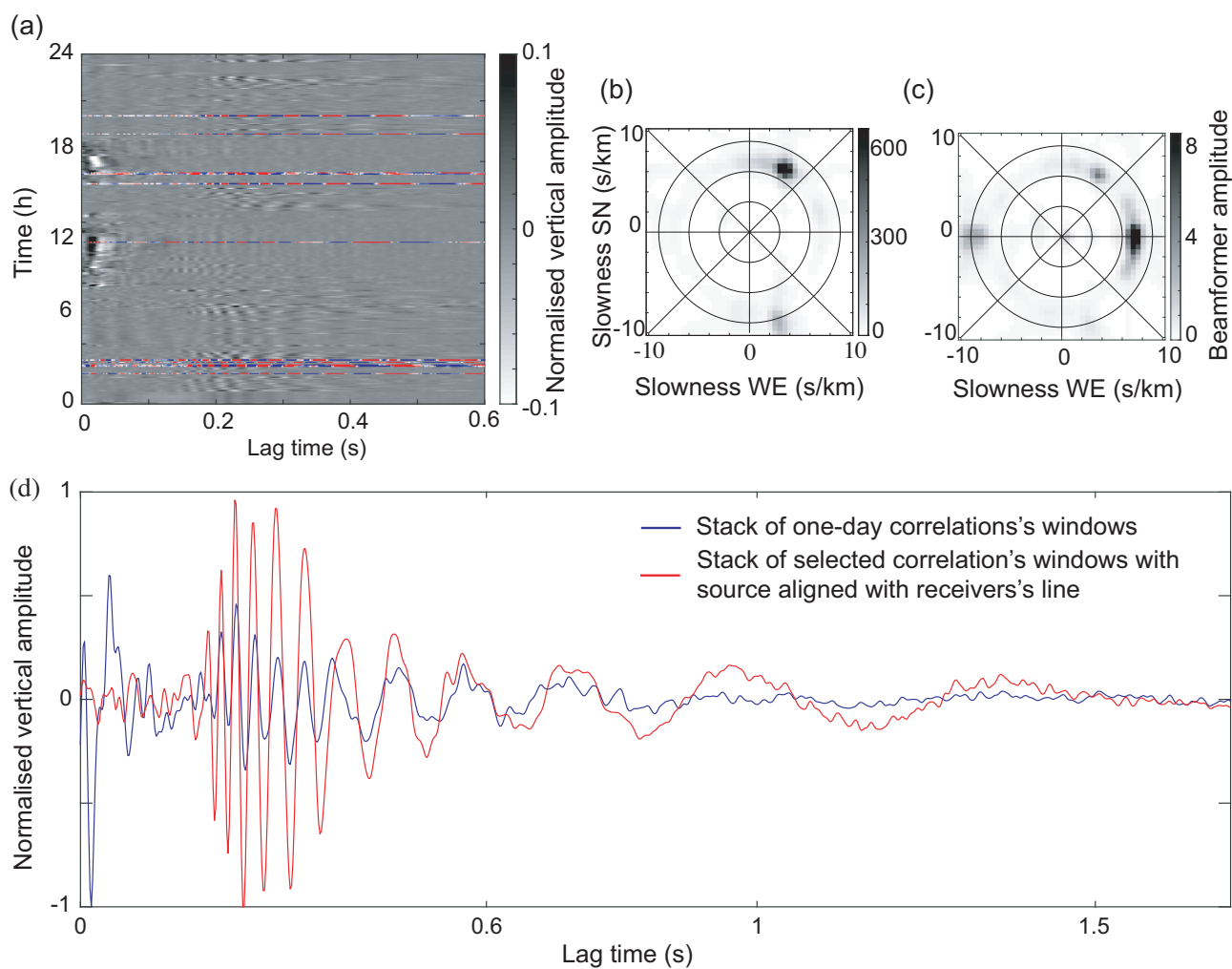
Figure 3. (a) Five-minute correlation windows as a function of time between the easternmost station of LAE and the central receiver of the EW sensors line, filtered between 1 Hz and 60 Hz. Correlations shown in color are those with the dominant source aligned with the EW line. The correlations were calculated from the ambient seismic wavefield recorded on March 9, 2019. (b) Beamforming calculated from the full day of ambient seismic noise recorded on March 9, 2019, in the [15-17] Hz frequency band. The noise sources are dominant in the northwest. (c) Beamforming from the summation of the 5-min seismic noise segments selected for an optimal NCF. The dominant noise sources are aligned with the EW line. (d) In blue: stack of the 288 correlations. In red: optimized NCF. The signal-to-noise ratio is significantly enhanced.

the context of geophysics on a floating ice layer in Moreau et al (2017) and Moreau, Boué et al (2020). As this processing has already been described several times in the literature, we only recall the main ideas here, and we invite the reader to refer to

160 the above three references for more details.

The linear arrays contain either two or four 3C geophones, which are considered as virtual sources for the calculation of the NCF. The classical way to obtain dispersion curves from a set of NCFs is to apply a Fourier transform to the time and space dimensions, which yields the frequency-wavenumber spectrum. When several virtual sources are available, the spectra can be averaged over the virtual sources.

165 A better way of taking advantage of the multiplicity of virtual sources consists of inserting a singular value decomposition to the matrix of the transmit-receive NCF between the Fourier transform on the time dimension and that on the space dimension. The singular vectors define an orthonormal basis of the space dimension along the receivers, where the modes decompose. Their relative intensity is contained in the singular values. This decomposition is performed at each frequency of the spectrum. To obtain the wavenumber, a spatial Fourier transform is applied directly on the singular vector associated to the most energetic

170 singular values at each frequency.

The interest of this processing is two-fold: (i) it is possible to separate signal from noise by applying a threshold to the singular values; and (ii) all modes stand out with the same spectral intensity (Fig. 4), despite their different relative intensities in the wavefield, because singular vectors have a unit norm. The dispersion curves can therefore be identified more clearly on a larger bandwidth (Moreau, Boué et al, 2020). In the present work, they are extracted from the spectrum by identification of

175 all of the frequency-wavenumber couples with a spectral intensity above a threshold. This threshold is set heuristically to 0.2, to achieve the best compromise between the visibility of the propagation modes and that of the seismic noise that pollutes our spectra. Based on this method, four sets of dispersion curves are extracted:

- from E to W with LAE as virtual sources;

- from W to E with LAW as virtual sources;

180 - from N to S with LAN as virtual sources;

- from S to N with LAS as virtual sources.

Finally, the dispersion curves obtained from propagations in opposite directions are averaged together to reduce uncertainties, in a similar fashion as in (Moreau & al, 2014b). This yields one dispersion curve per mode per day in the EW and NS lines. Next, the dispersion curves are inverted for the sea-ice properties.

185 ## 2.4 Estimation of sea-ice parameters with Bayesian inference

2.4.1 Forward model, parameterization of the problem, and cost function

In the following, we use the notation $k_m^{\text{type}}(f)$ to describe the frequency-wavenumber spectrum of a mode ($m = QS, QS_0, SH_0$) at frequency f. Type = "EW" and "NS" refer to wavenumbers obtained from the data in the EW and NS lines, respectively, and Type="syn" refers to synthetic wavenumbers obtained with the forward model. The forward model used here is that introduced

190 by Stein et al (1998), which describes the asymptotic behavior of the seismic wavefield in a thin ice sheet that is floating on an
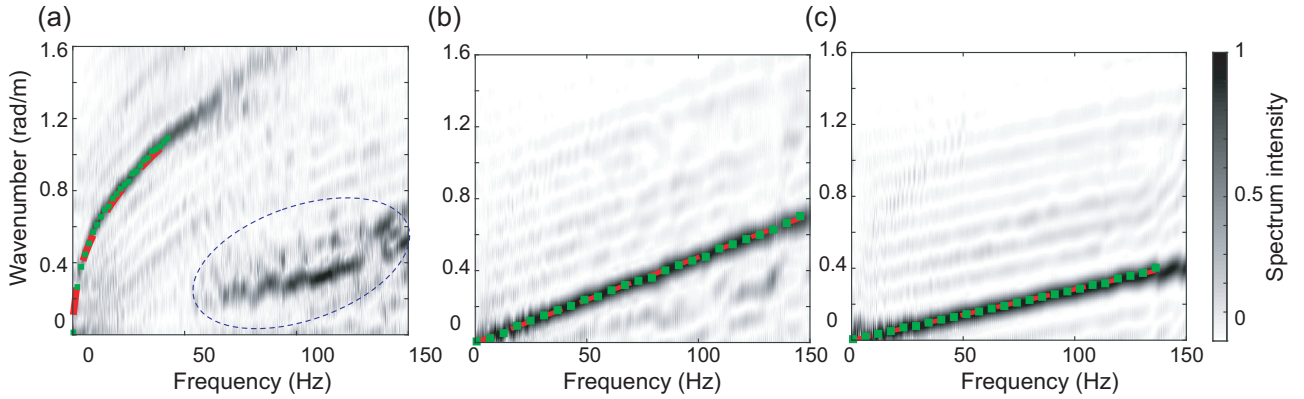
Figure 4. Frequency-wavenumber spectra obtained from the noise correlation function calculated on March 9, 2019, with the method described in section 2.2 and the processing of section 2.3, for recordings in the EW direction. (a) Spectrum from the vertical channel, dominated by the QS mode. The zone with a dotted contour highlights a seismic signature with slopes corresponding to a mix between the SH_0 and QS_0 modes. These modes appear on the vertical channel because the geophones were slightly tilted. (b) Spectrum from the radial channel, dominated by the QS_0 mode. (c) Spectrum from the transverse channel, dominated by the SH_0 mode. Green dots show the average of the dispersion curves extracted in the EW and WE directions. The red dotted lines show the dispersion curves obtained from Equations (1)-(3), with the sea-ice parameters inferred from Bayesian inference: $E = 4.1$ GPa, $\nu = 0.28$, $\rho = 917$ kg/m^3, and $h = 0.60$ m.

infinite water column, for low values of the product $f \cdot h$. While the depth of the lake is only about 10 m (Marchenko & al. , 2021), this is sufficient for the {ice-water} system not to behave like a bi-layer waveguide, because the first dispersive mode in an acoustic waveguide of thickness 10 m is evanescent under 75 Hz. The wavenumbers are obtained by solving the following equations:

195

$$k_{QS_0}(\omega) = \omega \sqrt{\frac{\rho(1-\nu^2)}{E}} \tag{1}$$

$$k_{SH_0}(\omega) = \omega \sqrt{\frac{2\rho(1+\nu)}{E}} \tag{2}$$

$$k_{QS}(\omega)^4 - \frac{h\rho\omega^2}{D} - \frac{\rho_w}{D} \left(\frac{\omega^2}{\sqrt{\left(\frac{k_{QS}(\omega)}{\omega}\nu\right)^2 - \left(\frac{\omega}{c_w}\right)^2}} - g \right) = 0. \tag{3}$$

200 In these equations, ω is the angular frequency, c_w and ρ_w are the speed of sound and density of the water, respectively, and $D = \frac{Eh^3}{12(1-\nu^2)}$ is the ice-bending rigidity.

Equation(1) holds as long as the QS_0 does not become dispersive, which occurs at $f \cdot h$ values above 500 Hz·m. The sampling frequency of the signals in this study is 500 Hz, so this condition is always satisfied. Equation(2) is always valid, because the

fundamental guided shear-horizontal mode, SH_0, is not dispersive. Equation(3) is valid when $f \cdot h$ remains less than about
50 Hz·m. The ice in the Van Mijen Fjord had a thickness of less than 0.8 m, hence this Equation(3) can be used at frequencies
up to ~65 Hz.

Given a dataset, $\mathbf{d}$, and a set of parameters for the ice layer, $\mathbf{X} = \{E, \nu, \rho, h\}$, a cost function can be defined as the L2 norm
between the wavenumbers calculated from the data and those calculated from Equations (1)-(3), such that:

$$f(\mathbf{d}, \mathbf{X}) = \frac{1}{3} \sum_{m=QS,QS0,SH0} \left\| k_m^{syn}(\omega) - k_m^{EW,NS}(\omega) \right\|, \tag{4}$$

where $\|.\|$ refers to the L2 norm. In Moreau, Boué et al (2020), E and ν were calculated directly from Equations (1) and (2),
assuming the density is known. Then h was estimated based on a grid search and forward modeling with the FE method. FE
modeling was used because it allows the inversion to be performed with high frequencies, of up to 100 Hz. The downside is
that it is computationally very expensive. In the present paper, instead of a FE model, we preferred to use Equation (3), which
is much more efficient, even though it means that we are limited to frequencies under 65 Hz for the QS mode. The benefits are
two-fold:

- First, compared to FE modeling, the efficiency of using Equation (3) allows inversions based on Bayesian inference, for h,
E, and ν, and also for ρ. The probability density function (PDF) of these parameters can be estimated and used to evaluate the
uncertainties of the inversions.

- Secondly, Equation (3) constrains mainly the thickness (to the power of three), but it also slightly constrains E, ν, and ρ (to a
unit power). Hence, the problem is better constrained when performing a joint inversion of all of the parameters simultaneously.

2.4.2 Estimation of the probability density function of the ice parameters with Bayesian inference

Solving the inverse problem consists of finding the parameters that best explain the data, based on the cost function defined in
Equation (4). This is a well-posed and well-constrained inverse problem, because there is a one-to-one relationship between
the model parameters and the global minimum of the cost function. We proceed with the Markov Chain Monte Carlo (MCMC)
algorithm (Metropolis et al, 1953), which provides an ensemble of solutions that fit the data with an acceptable level of
likelihood, given the data uncertainty. This ensemble of solutions is represented by the posterior distribution of the model
parameters, such that:

$$P(\mathbf{X}|\mathbf{d}) = \frac{P(\mathbf{d}|\mathbf{X}) P(\mathbf{X})}{P(\mathbf{d})}. \tag{5}$$

where $P(\mathbf{X}|\mathbf{d})$ is the likelihood function, $P(\mathbf{X})$ is the prior distribution, and $P(\mathbf{d})$ is the marginal likelihood function, which
is essentially a normalization factor. The posterior distribution expresses the conditional probability of the parameter values
based on evidence from measurements, expressed by the likelihood function, and from prior assumptions, expressed by the
prior distribution. It is also an estimate of the parameter PDF.

In the present problem, it is assumed that measurement errors are not correlated and are random, and thus that they can be modeled by a zero-mean Gaussian likelihood function with variance σ^2:

$$P(\mathbf{d}|\mathbf{X}) = \exp\left(-\frac{(f(\mathbf{d},\mathbf{X}))^2}{2\sigma^2}\right),\tag{6}$$

where σ^2 is the variance associated with the measurement errors. This is a typical likelihood function as used in many data-fitting problems (Tarantola, 2005). Moreover, it is also assumed for the prior distribution that the model parameters have equal probability over a finite range of values:

- E is between 2 GPa and 6 Gpa;

- ν is between 0.1 and 0.5;

- ρ is between 700 kg/m^3 and 1000 kg/m^3;

- h is between 0.15 m and 1.15 m.

Determining the optimal value of σ^2 is essential for appropriate sampling of the PDF. However, as this is data dependent, it cannot be set *a priori* for all of the inversions in this study. Moreover MCMC methods generally require a burn-in phase before reaching the posterior distribution. To tackle both of these issues, we precede the MCMC algorithm by simulated annealing (SA) global optimization (Kirkpatrick & al., 1983), to determine σ^2 and to improve convergence. Another approach consists of considering the variance as part of the inversion parameters of the MCMC algorithm, in what is know as trans-dimensional MCMC. However the method proposed in this paper has the advantage that it converges much faster, and it is robust for dealing with our dataset.

Simulated annealing is also an MCMC method. However, its aim is to converge on the global optimum rather than to generate samples from the posterior distribution. To this end, σ^2 in the likelihood function is initialized with a large value, to allow broad sampling of the parameter space. This value is slowly reduced with each iteration, in what is termed the "cooling schedule", and if a sufficiently gradual schedule is chosen, the algorithm will converge to the global optimum. In practice, the cooling schedule can be implemented in a number of ways. We use a standard schedule, T, where the variance is reduced from $T_0 = 0.05$ to $T_1 = 0.001$ in an exponential function such that:

$$T(n) = T_0\left(\frac{T_1}{T_0}\right)^{n/N}\tag{7}$$

(Moreau & al, 2014c; Gradon & al , 2019).

The number of iterations, N, is set to 20000 for the SA. The SA phase is stopped when the algorithm reaches a number of iterations equal to N, or when it has remained stuck at the same position in the search space for more than 200 successive iterations. The MCMC algorithm is then started, with 50000 iterations, from the position in the search space that minimizes the cost function during the SA phase, and with a variance equal to the minimal variance reached, increased by 1% (which translates to a 10% increase of the standard deviation). This increase is to avoid the MCMC algorithm from spending hundreds of iterations (like the SA) at the same position in the search space, which would be a sign of poor calibration.
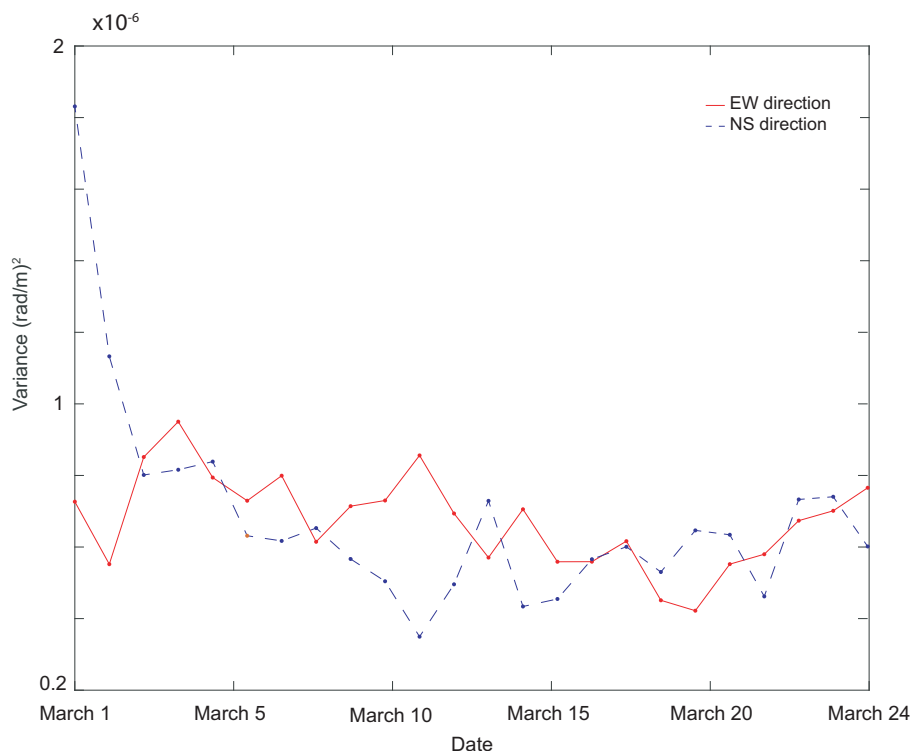
Figure 5. Daily evolution of the variance of measurement errors, estimated with the simulated annealing algorithm, as described in section 2.4.2. Variance in the EW (red) and NS (blue) directions. The variance in the EW direction remains stable, at around 0.5e-6. That in the NS direction appears to show a slightly decreasing pattern, which appears to be the consequence of temporal variations of the ice properties in this direction.

The variance is linked to measurement errors; *i.e.*, a mix between the influence of the SNR and other random perturbations

265 of the measure, such as variations in the physics of the problem. In the present problem, such perturbations are averaged when going from the time-space to the frequency-wavenumber domains, and thus the variance reflects variations of frequency-wavenumber values around ground truth values. Figure 4a-c indicates that the spread of the frequency-wavenumber couples is very narrow. Calculations of this spread show that it remains of the order of $\pm$ 0.002 rad/m, which corresponds to a maximal variance of about 4e-6 $(rad/m)^2$. This is consistent with the order of variances found with our method, as shown in Figure 5

270 for all of the days from March 1 to March 24, 2019. It appears stable around 0.5e-6 in the EW direction. In the NS direction, however, it shows a slight decrease. Since the SNR remains stable in the NCF, this decrease appears to be linked to temporal and spatial variations in the physics of the problem, which cannot be accounted for with the forward model. One of these is the influence of the snow layer on the seismic waveforms. In the NS direction, on March 1, the snow cover was thinner near LAS (about 10 cm) than it was near LAN (about 40 cm). Such variations were not noted in the EW direction, where the thickness

275 of the snow was more constant. Additional rainfall and snowfalls in March are likely to have influenced the propagation of the
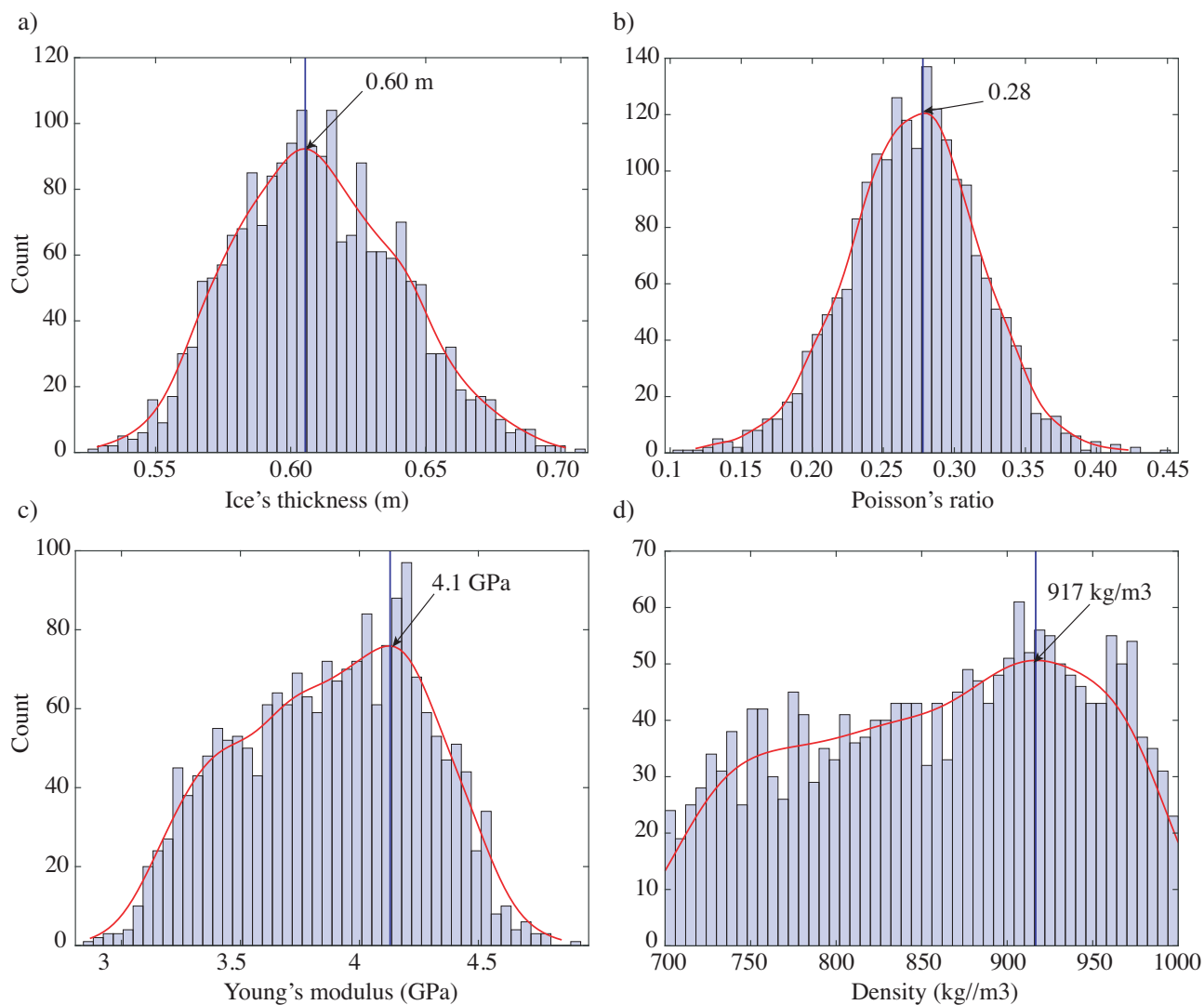
Figure 6. Example of the probability density function for E, h, ν, and ρ obtained after the inversion of the dispersion curves calculated on March 9, 2019, for LEW. The red curve is an estimate of the distribution of the PDF calculated from the kernel density estimator. The blue curve shows the maximum of our distribution. The Young's modulus, the ice thickness, and the Poisson's ratio are satisfactorily constrained by our method. The ice density is less well constrained, with a flatter distribution. The values obtained are nevertheless consistent with the literature.

seismic waves by modifying the apparent density and Young's modulus of the ice+snow system. This should be investigated in future studies, and forward modeling that accounts for a snow layer would represent significant progress.

After the MCMC algorithm has completed, a PDF is generated for E, h, ν, and ρ, and the estimated parameters correspond to their most likely values. Figure 6 shows an inversion result obtained for March 10, 2019, for LEW using our method.
280 The ice properties are determined from the histogram distribution obtained. We fit the distribution of the PDF from a kernel-type distribution density estimator (Fig.6, red curves). The maximum of this fit corresponds to the most probable value of the parameter (Fig. 6, blue curves). Figure 4 shows the theoretical dispersion curves (red dotted line) obtained with the PDF results; *i.e.*, $h = 0.60$ m, $E = 4.1$ GPa, $\nu = 0.28$, and $\rho = 917$ kg/m^3. We observe an excellent fit between the theoretical model and the wavefield data, which confirms the efficiency of our method. From the PDF, we find that the thickness, Young's modulus,
285 and Poisson's ratio are satisfactorily constrained, with standard deviations of 3 cm, 0.4 GPa, and 0.04, respectively. There is clear sharpening of the PDF around the most probable values. The PDF of the density, however, is not as sharp, with a standard deviation of about 80 kg/m^3. However, the values obtained from all of the inversions remain constant around $\rho = 915$ kg/m^3, which suggests that the actual standard deviation is not as high (Moreau, Boué et al, 2020).

3 Results and discussion

290 Sea ice is a complex material that is made up of solid ice, salt water, solid salts, and gases bubbles. In the Van Mijen Fjord, its growth is mainly controlled by the weather conditions *in situ*, but other factors are involved, such as: marine currents, which are mainly dominated by the tides; the supply of glacial freshwater from the surrounding mountains, which lowers the salinity of the water in the fjord (Hoyland , 2009); and warm Atlantic water from the West Spitsbergen Current (Gerland & al , 2006). The Van Mijen Fjord ice that we are studying is seasonal first-year ice, which disappears every summer, and it is covered by
295 snow.

The estimated parameters are of major importance for understanding and modeling sea-ice behavior. Thickness has a key role in coupled modeling (Allard & al , 2018), while the elastic parameters have key roles in recent rheological models (Dansereau & al , 2016). Figure 7 shows the evolution of the four parameters obtained by performing one inversion per day for the NS and EW sensor lines, and over a period from March 1 to 24, 2019.

300 In the field, a snow layer of 10 cm to 40 cm covers the ice. It is likely that this has an influence on our estimations, because guided modes propagate at a lower speed in snow than in ice. Hence, it is possible that some parameters might have been slightly under-estimated. However, is difficult to explicitly constrain the influence of the snow layer on our estimations, and this is left for a dedicated study.

The ice thickness is directly controlled by external environmental factors, such as: air temperature, snow type and depth,
305 wind speed, ocean heat flux, and surface radiation. For the EW direction, we observe a quasi-linear increase in ice thickness from March 1 to 24. The thickness varies from 55 ± 3 cm to 66 ± 3 cm. For the direction NS, we also observe an almost linear increase in ice thickness that ranges from 53 ± 4 cm to 63 ± 4 cm. These thickness values are consistent with the measurements made during the installation (about 60 cm) and de-installation (about 70 cm) of the array (Moreau, Boué et al, 2020), although
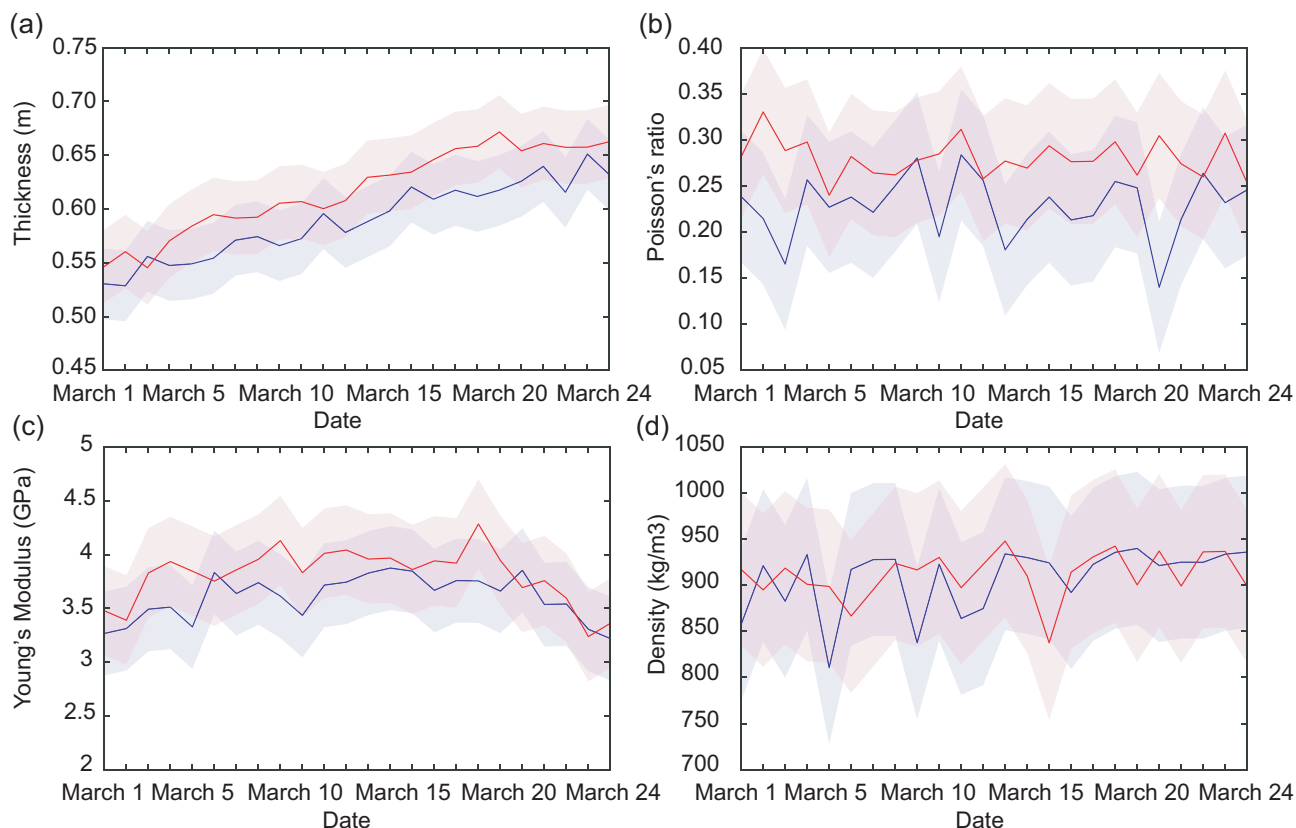
Figure 7. Daily evolution of the sea-ice parameters: (a) thickness, (b) Poisson's ratio, (c) Young's modulus, and (d) density, obtained for the lines of sensors in direction NS (blue) and EW (red). The coloured band represents the standard deviation associated with each of the curves. We observe an increase in the ice thickness in both directions, while the elastic parameters remain stable, around values that are consistent with the literature for first-year ice.

they are slightly lower. This difference can be explained by the presence of the snow on the ice. We suspect that the calculated

310   thickness could be under-estimated by 2 cm to 3 cm, but this falls within the uncertainty margins.

The Young's modulus depends on several parameters, such as salinity, porosity, and density of the ice. At Lake Vallunden, the ice contained a lot of brine, and was relatively porous and brittle for the first 30 cm; it was also covered with snow. All of these affected the speed of the guided modes, which propagate at a reduced speed compared to freshwater ice. The Young's modulus remains around $E = 3.7 \pm 0.4$ GPa for both directions.

315   The Poisson's ratio can be influenced by many factors too, such as loading rate, temperature, grain size, grain structure, direction of loading, and state of microcracking, among others. In view of the short study period, we therefore expect to have a relatively stable Poisson's ratio of around 0.28 ± 0.05 for the EW direction and 0.23 ± 0.05 for the NS direction.

Knowing the density of the ice and its thickness are crucial parameters for safe ice transport and the opening of new shipping routes. The salinity and porosity of the ice are factors that influence its density. The density of sea ice is not constant through the

320 ice thickness. It tends to be less dense in the freeboard. This is because air bubbles tend to accumulate in the upper part of the ice, while brine tends to accumulate in the lower part of the ice (Hoyland , 2009). The density is generally insensitive to temperature changes, which is consistent with our results. The inversions give a value that is very stable, at around $910 \pm 82 \ \mathrm{kg.m^{-3}}$ for the EW direction, and $908 \pm 80 \ \mathrm{kg.m^{-3}}$ for the NS direction.

From these inversion results, we note that the thickness, Young's modulus, and Poisson's ratio are very well constrained
325 by our method. All of our results appear to be compatible with relatively small thickness and young ice that insulates the heat fluxes rather poorly. The density parameter is a bit less well constrained. The PDF of the density has a more uniform distribution, and the uncertainty is larger than for the other parameters. Nevertheless, the actual uncertainty is probably much smaller, as all of the inversions give a very stable value, of around 910 kg/m^3 for the EW direction and 908 kg/m^3 for the NS direction. Moreover, the density values obtained are within a range confirmed by the literature (Timco and Frederking,
330 1996). In this sense, we can choose to perform the same inversions by fixing the density, on the assumption that we can better constrain the other parameters. In this way, we obtain the same results with smaller uncertainties. They are 0.1 GPa for the Young's modulus, 0.04 for the Poisson's modulus, and 2 cm for the ice thickness. As the results obtained are very close when the density is either fixed or not fixed, it appears scientifically very interesting to also invert the density parameter.

4   Conclusions

335 This paper introduces a methodology for estimating and monitoring the thickness, Young's modulus, density, and Poisson's ratio of sea ice in different directions, using the ambient seismic noise recorded with a seismic array. The methodology consists of extracting from the NCF, and then inverting, the dispersion curves of the guided modes propagating in sea. To calculate the daily NCF, we show that selecting the time windows where the dominant seismic source is aligned with the receivers significantly improves the SNR. This strategy also prevents potential directional bias from other dominant noise sources,
340 which would result in higher apparent modal velocity and corrupt the estimation of sea ice parameters. The dispersion curves of the three fundamental guided modes are inverted with MCMC sampling for inferring the probability density function of the sea ice parameters. We obtain satisfactory results that are consistent with the observations and measurements made *in situ*. Thus, we demonstrate that by using this method, it is possible to constrain the thickness, density, and elastic properties of sea ice both precisely and on a daily basis.

345 This approach could also be useful in various other fields, such as maritime transport safety or oceanography. The daily monitoring of ice thickness and stiffness offered by this method can help to ensure safe movement on sea ice in polar regions where the majority of the population travels by snowmobile. It can also open up possible new routes that were previously closed due to the lack of knowledge of these parameters. In the field of biology, for example, observations suggest that Meso-Zooplankton Biomass Density is closely related to variations in sea-ice properties.

350 In future works, another way of processing these seismic data is to exploit the thousands of icequakes present in the recordings, which arise from the natural cracking of the ice. These energetic and impulsive sources will allow the reconstruction of

the Green's function of the medium in a multitude of directions over time. This will form the basis for a temporally evolving three-dimensional tomographic profile of the sea ice beneath the seismic array, with applications for characterizing its rheology.

Author contributions. Ludovic Moreau designed and led the Icewaveguide experiment in the scope of the IWG project (ANR10 LABX56).
355 He supervised all this manuscript and research. Ludovic Moreau, Agathe Serripierri, Pierre Boue and Jérome Weiss participated in the deployment of the seismic array. Agathe Serripierri processed the data. Pierre Boue provided the code for computing correlations and beamforming. Philippe Roux contributed to the development of the methodology and supervised this research. Jérôme Weiss contributed to the interpretation of the results.

Competing interests. The authors declare that they have no conflict of interest.

360 *Acknowledgements.* ISTerre is part of Labex OSUG@2020 (ANR10 LABX56). This research was funded by the Agence Nationale de la Recherche (ANR, France) and by the Institut Polaire Français Paul-Emile Victor (IPEV).

References

Allard, R. A., S. L. Farrel, D. A. Hebert, W. F. Johnston, L. Li, N. T. Kurtz, M. W. Phelps, P. G. Posey, R. Tilling, A. Ridout, A. J. Wallcraft (2018), Utilizing CryoSat-2 sea ice thickness to initialize a coupled ice-ocean modeling system, *Advances in Space Research* 62(6):1265–1280

Anderson, D. L. (1958), Preliminary results and review of sea ice elasticity and related studies, *Trans. Eng. Inst. Canada* 2(3):2–8

Belter, H. J., T. Krumpen, S. Hendricks, J. Hoelemann, M. A. Janout, R. Ricker and C. Haas (2020), Satellite-based sea ice thickness changes in the Laptev Sea from 2002 to 2017: comparison to mooring observations, *The Cryosphere*, 14(7): 2189–2203

Campillo M. and A. Paul (2003), Long-range correlations in the diffuse seismic coda, *Science*, **299**(5606): 547–549

Dansereau V., J. Weiss, P. Saramito, P. Lattes A Maxwell elasto-brittle rheology for sea ice modelling, *The Cryosphere*, **10**(3): 1339–1359

Gerland S., R. Hall (2006), Variability of fast-ice thickness in Spitsbergen fjords *Annals of Glaciology* , 44:231–239

Gouédard, Pierre and Roux, Philippe and Campillo, Michel and Verdel, Arie, Convergence of the two-point correlation function toward the Green's function in the context of a seismic-prospecting data set, *Geophysics*, **73**(6): V47–V53

Gradon, C. (2019), L. Moreau, P. Roux, and Y. Ben-Zion Analysis of surface and seismic sources in dense array data with match field processing and Markov chain Monte Carlo sampling *Geopys. J. Int.*, 218 (2):1044—1056

De Verdière, Y. C. (2006), Mathematical models for passive imaging I: general background *arXiv preprint math-ph/0610043*

Høyland K. V., Ice thickness, growth and salinity in Van Mijenfjorden, Svalbard, Norway *Polar Research* 28(3):339–352

Hunkins, K. (1960), Seismic studies of sea ice, *J. Geophys. Res.* 65(10):3459—3472

Kirkpatrick, S., Gelatt, C., Vecchi, M. (1983), Optimization by Simulated Annealing. *Wire.* 220(4598):671—680

Kwok, R. and G.F. Cunningham, (2008), ICESat over Arctic sea ice: Estimation of snow depth and ice thickness, *J. Geophys. Res. Oceans*, 113(C8)

Kwok, R. (2010), Satellite remote sensing of sea-ice thickness and kinematics: a review, *J. Glaciol*, 56(200): 1129-—1140

Lamb, H. (1917) On waves in an elastic plate, *Proceedings of the Royal Society of London. Series A, Containing papers of a mathematical and physical character* , 93(648): 114–128

Lindasy, R and A. Schweiger (2015), Arctic sea ice thickness loss determined using subsurface, aircraft, and satellite observations, *The Cryosphere*, 9(1): 269–283

Lobkis, O. I.,R. L. Weaver (2001), On the emergence of the Green's function in the correlations of a diffuse field, *The Journal of the Acoustical Society of America*, 110(6): 3011–3017

Marchenko, A.V., E. G. Morozov, A.V. Ivanov, T.G. Elizarova, D.I., Frey (2021), Ice thickening caused by freezing of tidal jet, *Russian Journal of Earth Sciences*, 21(2): ES2004–ES2004

Marsan, D., J. Weiss, E. Larose, and J.-P. Métaxian (2012) Sea-ice thickness measurement based on the dispersion of ice swell, *J. Acoust. Soc. Am.*, 131(1): 80–91

Marsan, D., J. Weiss, L. Moreau, F. Gimbert, M. Doble, E. Larose and J. Grangeon (2019), Characterizing horizontally-polarized shear and infragravity vibrational modes in the Arctic sea ice cover using correlation methods, *J. Acoust. Soc. Am.*, 145(3): 1600–1608

Metropolis, N., A. W. Rosenbluth, M. N. Rosenbluth, A. H. Teller, E. Teller (1953), Equation of state calculations by fast computing machines, *The journal of chemical physics*, 21(6): 1087–1092

Minonzio J.-G., M. Talmant, and P. Laugier (2010), Guided wave phase velocity measurement using multi-emitter and multi-receiver arrays in the axial transmission configuration. *J. Acoust. Soc. Am.*, 127(5): 2913–2919

Moreau L., J.-G. Minonzio, M. Talmant, and P. Laugier (2014a), Measuring the wavenumber of guided modes in waveguides with linearly
400   varying thickness. *J. Acoust. Soc. Am.*, 135(5): 2614–2624

Moreau L., J.-G. Minonzio, M. Talmant, J. Foiret, E. Bossy and P. Laugier (2014b), Accurate measurement of guided modes in a plate using
    a bidirectional approach. *J. Acoust. Soc. Am.*, 135(1): EL15-EL21

Moreau L., A. J. Hunter, A. Velichko and P. D. Wilcox (2014), 3-D reconstruction of sub-wavelength scatterers from the measurement of
    scattered fields in elastic waveguides. *IEEE transactions on ultrasonics, ferroelectrics, and frequency control*, 61(11): 1864–1879

405 Moreau, L., C. Lachaud, R. Théry, M. V. Predoi, D. Marsan, J. Weiss and M. Montagnat (2017), Monitoring ice thickness and elastic
    properties from the measurement of leaky guided waves: A laboratory experiment *J. Acoust. Soc. Am.*, 142(5): 2873—2880

Moreau, L., RESIF (2019), Svalbard − Vallunden (Icewaveguide) (RESIF − SISMOB_Nodes) [$Dataset$]. RESIF − Réseau Sismologique
    et géodésique Français, https://doi.org/10.15778/RESIF.XG2019,

Moreau, L., P. Boué, A. Serripierri, J. Weiss, D. Hollis, I. Pondaven, B. Vial, S. Garambois, E. Larose, A. Helmstetter, L. Stehly, G. Hillers,
410   and O. Gilbert (2020), Sea ice thickness and elastic properties from the analysis of multimodal guided wave propagation measured with a
    passive seismic array, *J. Geophys. Res-Oceans*, 125(4): e2019JC015709

Moreau, L., J. Weiss, and D. Marsan (2020), Accurate Estimations of Sea-Ice Thickness and Elastic Properties From Seismic Noise Recorded
    With a Minimal Number of Geophones: From Thin Landfast Ice to Thick Pack Ice, *J. Geophys. Res-Oceans*, 125(11): e2020JC016492

Mu, L., M. Losch, Q. Yang, R. Ricker, S. N. Losa and L. Nerger (2018), Arctic-Wide Sea Ice Thickness Estimates From Combining Satellite
415   Remote Sensing Data and a Dynamic Ice-Ocean Model with Data Assimilation During the CryoSat-2 Period, *J. Geophys. Res. Oceans*,
    123(11): 7763—-7780

Petty, A.A., N.T. Kurtz, R. Kwok, T. Markus, T.A. Neumann (2020), Winter Arctic sea ice thickness from ICESat-2 freeboards, *J. Geophys.
    Res. Oceans*, 125(5)

Rampal, P., J. Weiss, C. Dubois, J.-M. Campin (2011), IPCC climate models do not capture Arctic sea ice drift acceleration: Consequences
420   in terms of projected sea ice thinning and decline, *J. Geophys. Res. Oceans*, 116(C8)

Ricker, R., S. Hendricks, V. Helm, H. Skourup and M. Davidson (2014), Sensitivity of CryoSat-2 Arctic sea-ice freeboard and thickness on
    radar-waveform interpretation, *The Cryosphere*, 8(4): 1607–1622

Romeyn, R., A., Hanssen, B.O. Ruud and T. A., Johansen (2021), Sea ice thickness from air-coupled flexural waves, *The Cryosphere*, 15:
    2939–2955

425 Rost, S., C. Thomas (2002), Array seismology: Methods and applications, *Reviews of geophysics*, 40(3): 2–1

Roux, P., WA., Kuperman, NPAL Group (2004), Extracting coherent wave fronts from acoustic ambient noise in the ocean, *The Journal of
    the Acoustical Society of America*, 116(4): 1995–2003

Sabra, K.G., P. Gerstoft, P. Roux, W.A. Kuperman and M.C. Fehler (2005), Extracting time-domain Green's function estimates from ambient
    seismic noise, *Geophys. Res. Lett* 32(3): 79-—84

430 Stein, P. J., S. E. Euerle, , and J. C. Parinella (1998), Inversion of pack ice elastic wave data to obtain ice physical properties, *J. Geophys.
    Res.* 103(C10): 21783–21796

Sambridge, M. et Mosegaard, K. Monte Carlo methods in geophysical inverse problems, *Reviews of Geophysics* 40(3): 3–1

Screen, J.A. and C. Deser, Pacific Ocean variability influences the Time of Emergence of a seasonally ice-free Arctic ocean, *Geophys. Res.
    Lett.*46(4): 2222–2231

435 Shapiro, N. M. and M. Campillo (2004), Emergence of broadband Rayleigh waves from correlations of the ambient seismic noise, *Geophys.
    Res. Lett.*, 31(7)

Steffen, W., J. Rockström, K. Richardson, T. M. Lenton, C. Folke, D. Liverman, C. P. Summerhayes, A. D. Barnosky, S. E. Cornell, and M. Crucifix (2018), Trajectories of the Earth System in the Anthropocene *Proceedings of the National Academy of Sciences,* 155(33): 8252–8259

440 Stroeve, J., M. M. Holland, W. Meier, T. Scambos, and M. Serreze (2007), Arctic sea ice decline: Faster than forecast, *Geophys. Res. Lett.*, 34(9)

Stroeve, J. C., V. Kattsov, A. Barrett, M. Serreze, T. Pavlova, M. Holland, and W. N. Meier (2012), Trends in Arctic sea ice extent from CMIP5, CMIP3 and observations, *Geophys. Res. Lett.*, 39(16)

Tarantola, A. (2005), Inverse Problem Theory and Methods for Model Parameter Estimation, Society for Industrial and Applied Mathematics, 445 Philadelphia, Pennsylvania.

Timco, G. W. and R. M. W. Frederking (1996), A review of sea ice density, *Cold regions science and technology* 24(1): 1–6

Wadhams, P. (2012) Arctic Ice Cover, Ice Thickness and Tipping Points, *Ambio*, 41(1): 23–33

Yang, T. C. and G. R. Giellis (1994), Experimental characterization of elastic waves in a floating ice sheet, *Bull. Amer. Meteorol. Soc.* 83(2): 255–276